AGU PUBLICATIONS

JGR

Journal of Geophysical Research: Planets

RESEARCH ARTICLE
10.1002/2017JE005262

Special Section:
Investigations of the Bagnold Dune Field, Gale crater

Mineralogy of an active eolian sediment from the Namib dune, Gale crater, Mars

C. N. Achilles[1], R. T. Downs[1], D. W. Ming[2], E. B. Rampe[2], R. V. Morris[2], A. H. Treiman[3], S. M. Morrison[1], D. F. Blake[4], D. T. Vaniman[5], R. C. Ewing[6], S. J. Chipera[7], A. S. Yen[8], T. F. Bristow[4], B. L. Ehlmann[8,9], R. Gellert[10], R. M. Hazen[11], K. V. Fendrich[12], P. I. Craig[3], J. P. Grotzinger[9], D. J. Des Marais[4], J. D. Farmer[13], P. C. Sarrazin[14], and J. M. Morookian[8]

[1]Department of Geosciences, University of Arizona, Tucson, Arizona, USA, [2]Astromaterials Research and Exploration Science Division, NASA Johnson Space Center, Houston, Texas, USA, [3]Lunar and Planetary Institute, Houston, Texas, USA, [4]NASA Ames Research Center, Moffett Field, California, USA, [5]Planetary Science Institute, Tucson, Arizona, USA, [6]Department of Geology and Geophysics, Texas A&M University, College Station, Texas, USA, [7]Chesapeake Energy, Oklahoma City, Oklahoma, USA, [8]Jet Propulsion Laboratory, California Institute of Technology, Pasadena, California, USA, [9]Division of Geological and Planetary Sciences, California Institute of Technology, Pasadena, California, USA, [10]Department of Physics, University of Guelph, Guelph, Ontario, Canada, [11]Geophysical Laboratory, Carnegie Institution, Washington, District of Columbia, USA, [12]Department of Earth and Planetary Sciences, American Museum of Natural History, New York, New York, USA, [13]School of Earth and Space Exploration, Arizona State University, Tempe, Arizona, USA, [14]SETI Institute, Mountain View, California, USA

Key Points:
- Gobabeb is dominated by basaltic minerals (~60%) and X-ray amorphous phases (~40%) and likely derives from more than one parent material
- CheMin-derived crystal chemistry provides insights into the origin(s) and geologic history of the dune material
- CheMin analyses of Gobabeb confirm inferences of mafic-enriched sands and allow for an evaluation of orbital-based mineralogy estimates

Correspondence to:
C. N. Achilles,
cheriea@email.arizona.edu

Citation:
Achilles, C. N., et al. (2017), Mineralogy of an active eolian sediment from the Namib dune, Gale crater, Mars, *J. Geophys. Res. Planets*, *122*, 2344–2361, doi:10.1002/2017JE005262.

Received 14 JAN 2017
Accepted 7 JUN 2017
Accepted article online 15 JUN 2017
Published online 30 NOV 2017

Abstract The Mars Science Laboratory rover, Curiosity, is using a comprehensive scientific payload to explore rocks and soils in Gale crater, Mars. Recent investigations of the Bagnold Dune Field provided the first in situ assessment of an active dune on Mars. The Chemistry and Mineralogy (CheMin) X-ray diffraction instrument on Curiosity performed quantitative mineralogical analyses of the <150 μm size fraction of the Namib dune at a location called Gobabeb. Gobabeb is dominated by basaltic minerals. Plagioclase, Fo56 olivine, and two Ca-Mg-Fe pyroxenes account for the majority of crystalline phases along with minor magnetite, quartz, hematite, and anhydrite. In addition to the crystalline phases, a minimum ~42 wt % of the Gobabeb sample is X-ray amorphous. Mineralogical analysis of the Gobabeb data set provides insights into the origin(s) and geologic history of the dune material and offers an important opportunity for ground truth of orbital observations. CheMin's analysis of the mineralogy and phase chemistry of modern and ancient Gale crater dune fields, together with other measurements by Curiosity's science payload, provides new insights into present and past eolian processes on Mars.

1. Introduction

The Mars Science Laboratory (MSL) rover, Curiosity, is providing in situ sedimentological, geochemical, and mineralogical assessments of rocks and sediment in Gale crater, Mars. Since landing in 2012, Curiosity has traveled over 16 km while exploring the sedimentary units of Aeolus Palus (Bradbury group) and the foothills of Aeolis Mons, commonly called Mount Sharp. Curiosity's recent traverse through an active basaltic eolian deposit, informally named the Bagnold Dune Field (Figure 1), provided the opportunity for a multi-instrument investigation of the geomorphology, chemistry, and mineralogy of the dunes. This comprehensive campaign is the first in situ assessment of active dunes on a planet other than Earth [*Bridges and Ehlmann*, 2017].

Prior to Curiosity's arrival at the Bagnold Dune Field, orbital observations characterized the geomorphology and predicted the mineralogy of the Bagnold Dunes. HiRISE (High Resolution Imaging Science Experiment) images revealed that the dune field is composed of barchan, crescentic, and linear dunes with active ripple and dune migration resulting from a combination of northwesterly and northeasterly winds [*Hobbs et al.*, 2010; *Silvestro et al.*, 2013; *Day and Kocurek*, 2016]. Visible-near-infrared (VNIR) and midinfrared (MIR) spectral data indicated strong olivine and high-calcium pyroxene signatures [*Rogers and Bandfield*, 2009; *Anderson and Bell*, 2010; *Milliken et al.*, 2010; *Seelos et al.*, 2014] and a predicted olivine composition of Fo55(5) [*Lane and Christensen*, 2013]. Values in parentheses indicate precision in the last digit and 1σ uncertainty (i.e., Fo55 ± 5). Mapping of VNIR data showed a greater abundance of olivine in the barchan dunes and a greater abundance of high-Ca pyroxene in the linear dunes, implying spatially variable mineral sorting within the

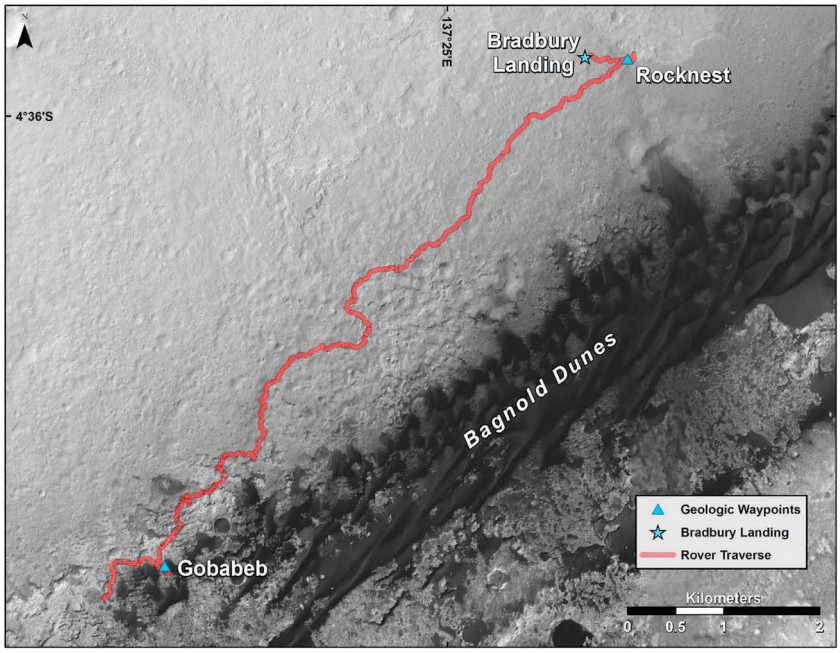

Figure 1. MSL traverse map indicating the location of the two eolian deposits, Rocknest and Gobabeb, measured by the rover's full instrument suite.

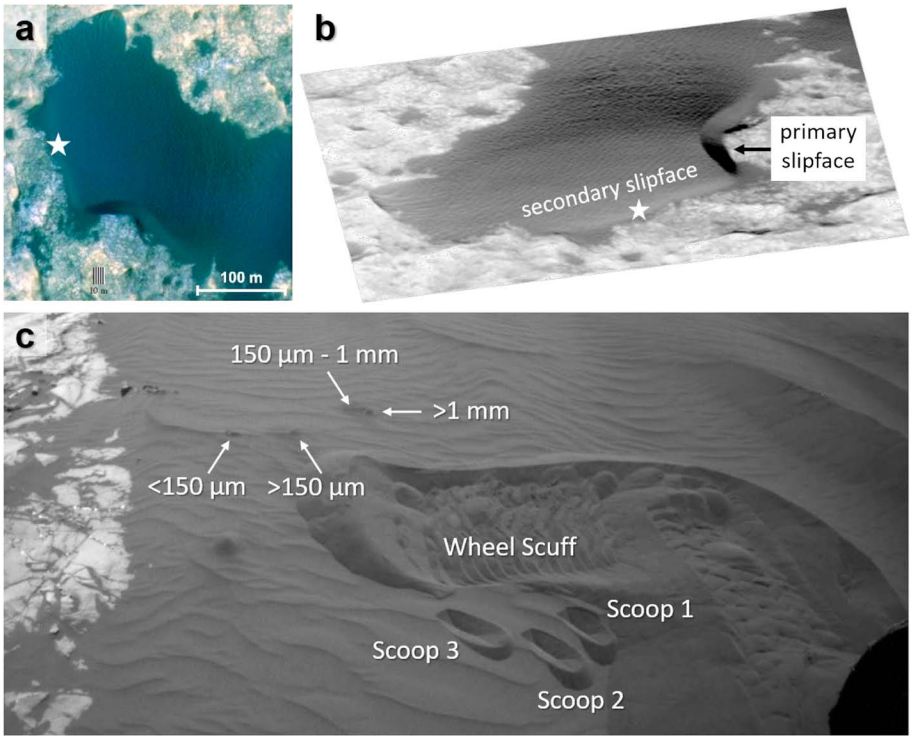

Figure 2. (a) HiRISE image (NASA Photojournal #PIA19930) of the Namib dune (top left) and location of the Gobabeb sample site (star). (b) Perspective view of the area pictured in Figure 2a indicating primary and secondary slipfaces. (c) Front Hazcam image (FLB_506861868) from sol 1232 of the Gobabeb worksite. Locations of the wheel scuff, three scoop sites, and four sieved sample piles are labeled. Wheel scuff width is ~0.5 m.

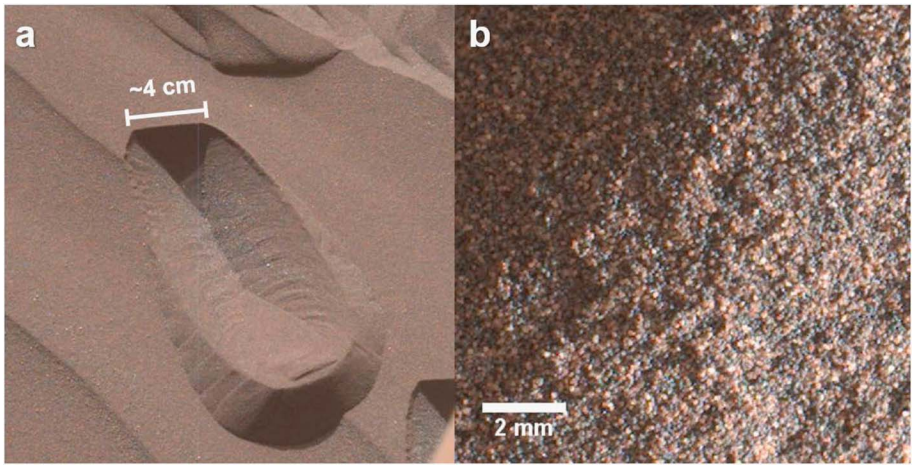

Figure 3. (a) Mastcam image of the Gobabeb trench (sol 1231, mcam03794). (b) MAHLI image of the Gobabeb <150 μm dump pile (sol 1226, mhli03249).

dune field [*Seelos et al.*, 2014; *Lapotre et al.*, 2017]. Curiosity's traverse through the Bagnold Dune Field presents a rare opportunity to provide mineralogical ground truth for this type of orbital observation.

The science objectives of the Bagnold Dune Campaign included characterizing sedimentary structures and active dune processes on Mars, constraining the provenance of the dune sand, and assessing the potential of the dunes as a trap for water [*Bridges and Ehlmann*, 2017]. From sols (Mars days) 1164 to 1244, Curiosity completed six campaign phases, including an in situ sampling campaign that was conducted at a site named Gobabeb (Figure 1), located on the northwestern flank and secondary slipface of the Namib barchan dune (Figure 2). The Gobabeb site was chosen for its strong olivine spectral signature and high rates of sediment transport, as evidenced by large ripple displacements [*Lapotre et al.*, 2016; *Silvestro et al.*, 2016]. Three scooped samples were collected from the crest of a large ripple (Figures 2 and 3). During the Bagnold sampling campaign, observations were designed to characterize the grain size distribution, chemical composition, mineralogy, and volatile chemistry of the three scooped samples [*Cousin et al.*, 2017; *Ehlmann et al.*, 2017; *O'Connell-Cooper et al.*, 2017].

Gobabeb is the second eolian sand deposit investigated with Curiosity's full suite of science instruments. The first, named Rocknest, is an inactive, dust-covered sand shadow (Figure 4) [*Bish et al.*, 2013; *Blake et al.*, 2013]. Rocknest is dominated by basaltic minerals, has a substantial fraction (35(15) wt %) of X-ray amorphous

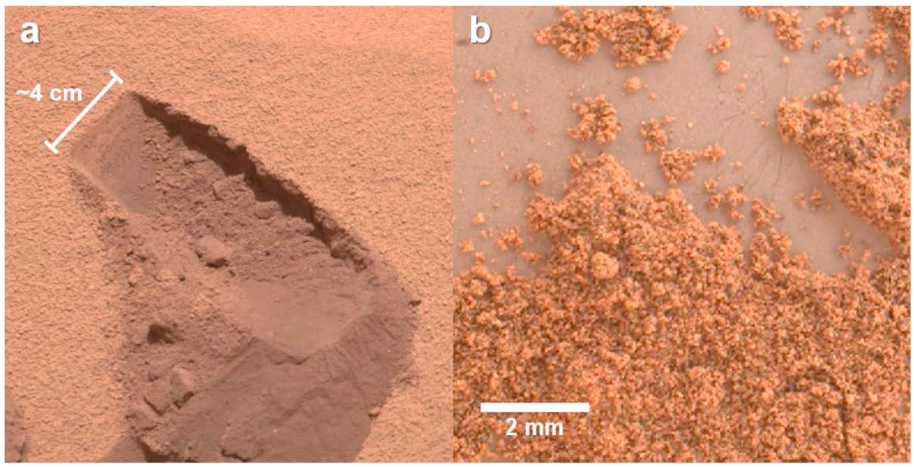

Figure 4. (a) Mastcam image of the Rocknest trench (sol 93, mcam04327). (b) MAHLI image of the Rocknest <150 μm sample on the observation tray (sol 95, mhli01120). The Rocknest site has an armored coating and higher dust content giving the surface of the sediment a more reddish hue compared to Gobabeb.

materials, and a bulk elemental composition similar to basaltic sediments analyzed elsewhere on Mars by the Mars Exploration Rovers (MERs). Comparisons of Rocknest and Gobabeb mineralogy provide insights into the provenance, source material(s), and weathering history of these modern dune forms. Shortly after the Gobabeb campaign, Curiosity analyzed lithified Stimson formation sandstones, interpreted to be ancient (>3.7 Ga) sand dunes overlying Murray formation lacustrine mudstones [*Grotzinger et al.*, 2015; *Banham et al.*, 2016]. Taken together, Curiosity's characterization of both modern and ancient eolian deposits contributes to our understanding of the geologic history and environment of Gale crater as well as planet-wide eolian processes. Characterizing the mineralogy of Gale crater sands also provides an opportunity to contextualize our understanding of the nature of eolian deposits analyzed by previous Mars missions.

Prior to MSL, the chemical compositions of Martian soils had been analyzed by six landers (i.e., Viking I and II, Pathfinder, Spirit, Opportunity, and Phoenix) at sites distributed across the planet. Soils (defined here as loose, unconsolidated material) analyzed by the Viking landers in Utopia Planitia and Chryse Planitia had nearly identical compositions with the exception of a slight enrichment of Ti and Cl and depletion of S at Chryse Planitia [*Clark et al.*, 1982]. Pathfinder's exploration of a second site in Chryse Planitia showed soil compositions similar to both Viking sites [*Rieder et al.*, 1997]. Soils trenched by the Phoenix lander confirmed the presence of carbonate and perchlorate as trace components; however, the bulk soil composition was not measured [*Boynton et al.*, 2009; *Hecht et al.*, 2009; *Cannon et al.*, 2012; *Sutter et al.*, 2012].

Over the course of their multiyear missions, the Mars Exploration Rovers, Spirit and Opportunity, analyzed dozens of soils in Gusev crater and Meridiani Planum, respectively [*Yen et al.*, 2006]. Compositional similarities between basaltic soils at these two regions and those measured by previous landers indicate that many of Mars' equatorial soils contain some globally distributed components, specifically fine dust (particles <10 μm as defined by *Greeley and Iversen* [1985]) [*Yen et al.*, 2005]. The mineralogy of MER-analyzed soils was calculated from MIR spectral deconvolutions, normative geochemical calculations, and Mössbauer spectroscopy, but these techniques have limitations in distinguishing between compositionally similar phases, identifying non-Fe-bearing phases, detecting trace phases, and determining crystal chemistry [*Ming et al.*, 2006; *Morris et al.*, 2008; *Rogers and Aharonson*, 2008; *McSween et al.*, 2010]. The addition of X-ray diffraction with the Chemistry and Mineralogy (CheMin) instrument on the MSL payload provides the first comprehensive assessment of rocks and soils using X-ray crystallography to determine mineral phases, abundances, and chemistry.

Since landing, the chemical composition of Gale crater rocks and soils has been analyzed by the Alpha-Particle X-ray Spectrometer (APXS) [*Gellert et al.*, 2015; *Thompson et al.*, 2016], the ChemCam Laser-Induced Breakdown Spectrometer (LIBS) [*Maurice et al.*, 2012], and the Sample Analysis at Mars (SAM) instrument suite [*Mahaffy et al.*, 2012]. The legacy of APXS instruments on multiple Mars rover payloads (Pathfinder, Spirit, Opportunity, and Curiosity) provides direct comparisons of the geochemistry of soils across the Martian surface [*O'Connell-Cooper et al.*, 2017].

CheMin's analysis of Rocknest allowed for the first direct quantitative mineralogical comparison of Martian soils with the estimated modal mineralogies provided by the Spirit and Opportunity rovers. As a result of the striking similarity between the measured and estimated mineralogies, Rocknest is considered to be typical of Martian soils [*Bish et al.*, 2013; *Blake et al.*, 2013]. In this paper, we present the mineralogy and chemical composition of the Gobabeb <150 μm size fraction as measured by CheMin. Similarities and differences between Gobabeb, Rocknest, and other modern soils measured by Spirit and Opportunity [*Yen et al.*, 2005; *Ming et al.*, 2008; *Blake et al.*, 2013], as well as an ancient eolian bed form sampled by Curiosity [*Yen et al.*, 2017], will be discussed.

2. Methods

To meet the Bagnold Dune Campaign objectives, a sampling plan was implemented at the Gobabeb site. The area from which three samples were collected is characterized by small ripples, interpreted as wind impact ripples (Figure 2) [*Lapotre et al.*, 2016]. Because grain sorting processes concentrate the coarser fraction of sand at the ripple crests, target scoop locations were planned to capture material adjacent to these ripple crests. This strategy ensured the capture of a representative sample of dune sand. Scoop 1 was sieved to <150 μm and >150 μm size fractions, and a portion of the <150 μm sample was delivered to CheMin and SAM. Scoop 2 was sieved to 150 μm to 1 mm and >1 mm fractions, and a portion of the >150 μm to

1 mm fraction was delivered to SAM. Lastly, a sample from scoop 3 was intended for an additional delivery to SAM; however, this activity was not completed. The four sieved fractions were deposited in separate piles for imaging and chemical analyses (Figure 2).

Grain size distribution analyses were determined from Mars Hand Lens Imager (MAHLI) images of the four sieved fractions. Results from these analyses are described in *Cousin et al.* [2017] and *Ehlmann et al.* [2017]. Based on the material collected from scoops 1 and 2, the bulk Gobabeb deposit is composed of grains ~50 μm to 500 μm. Grains from the CheMin-measured <150 μm fraction range from ~45 μm to ~220 μm with an average size of 103 μm and 142 μm (when measured on the intermediate and long axis, respectively) [*Cousin et al.*, 2017; *Ehlmann et al.*, 2017].

The mineralogy and chemical composition of the Gobabeb sediment were characterized by the CheMin, SAM, ChemCam, and APXS instruments. Each scoop sample was processed by the Sample Acquisition Sample Processing and Handling (SA/SPaH) and the Collection and Handling for In situ Martian Rock Analysis (CHIMRA) systems to generate sieved fractions [*Anderson et al.*, 2012]. A portion of the <150 μm fraction from scoop 1 was delivered to CheMin. The CheMin instrument returns both X-ray diffraction (XRD) patterns and X-ray fluorescence (XRF) spectra of the samples it analyzes. However, CheMin's transmission geometry limits the usefulness of the XRF data due to sample self-absorption of X-ray photons below ~3 keV ($Z < 19$). A proxy measurement of bulk composition for the material analyzed by CheMin can be obtained from APXS data. For this reason, this study will make comparison principally from APXS analyses; LIBS measurements acquired at a finer spatial scale are presented in *Cousin et al.* [2017].

APXS analyzed the bulk Gobabeb sand and the four size fractions described above [*Ehlmann et al.*, 2017; *O'Connell-Cooper et al.*, 2017]. Results presented here will utilize APXS elemental analyses of the <150 μm fraction because this best represents the sample analyzed by CheMin.

2.1. APXS Geochemical Analyses

APXS provides the chemical compositions of rocks and soils by X-ray fluorescence spectroscopy using a ^{244}Cm radioactive source to irradiate the samples and a silicon diode detector to detect fluoresced X-rays. The MSL APXS instrument can detect and quantify the elements Na to Br (with characteristic X-ray energies between ~0.7 and ~25 keV [*Thompson et al.*, 2016]). The initial Gobabeb APXS analysis was made of soil disturbed by the rover wheel and is considered to represent the bulk dune composition. Following delivery of a portion of the <150 μm fraction to CheMin, the remaining sieved material was dumped for analysis by APXS; these APXS data are considered to be the representative bulk composition of the CheMin analyzed sample. The chemistry of the other three fractions analyzed by APXS is presented in *O'Connell-Cooper et al.* [2017].

2.2. CheMin X-ray Diffraction and X-ray Fluorescence Measurements

The CheMin XRD/XRF instrument produces diffraction patterns of soils or powders from drilled rock samples [*Blake et al.*, 2012]. Soils and powders are sieved to <150 μm and a portion is delivered to one of the instrument's 27 reusable sample cells. Positioned in pairs at the ends of tuning forks, the cells hold sample material between two polymer (Mylar or Kapton) windows. A piezoelectric actuator drives the tuning fork at resonance, and the resulting vibration causes a convective flow of sample material, randomizing grain orientations, and minimizing orientation effects. The instrument utilizes transmission geometry with a Co X-ray source (λ = 1.7902758 Å) collimated to a 70 μm diameter X-ray beam. An X-ray sensitive charge-coupled device (CCD) collects two-dimensional (2-D) XRD images over 10 to 30 h of analysis. The CCD detector is operated in single-photon counting mode and can be used to measure the amount of charge generated by each photon (and hence its energy). Diffracted CoKα X-ray photons are identified by their energy and are summed to yield a 2-D energy-discriminated CoKα diffraction pattern (Figure 5). All detected photons are summed into a histogram that represents an XRF spectrum of the sample.

During CheMin's initial analysis of Rocknest, the team found that sample material was ejected from the cell at even the lowest direct vibration intensity. As a result, the CheMin team employs indirect cell vibration for soil samples by activating the piezo driver in an adjacent cell pair to the one being analyzed. This gentler vibration method (also called "kumbayatic mode" [*Downs and MSL Science Team*, 2015]) was the method utilized for the majority of Rocknest and Gobabeb analyses. A previously used but empty Mylar sample cell, 7A, was chosen for the Gobabeb sample. This cell had been used for a sample of the Rocknest sand (scoop 5) from sols 94 to 151. After that cell was emptied on sol 151, a postdump, empty-cell analysis showed no

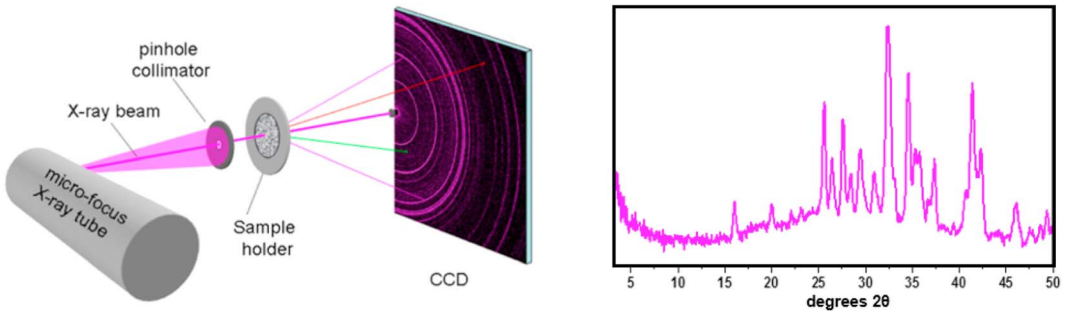

Figure 5. CheMin instrument configuration. Diffracted characteristic X-rays collect on the CCD result in a 2-D image (center) that is converted to a 1-D diffraction pattern (right). Modified from *Blake et al.* [2012].

significant residue from Rocknest. Thirty hours of data were collected from the Gobabeb sample using indirect vibration on sols 1236, 1240, 1245, and 1256.

The 2-D XRD images are converted to 1-D diffraction patterns (Figure 5) for analysis using a modification of the open-source GSE_ADA software [*Dera et al.*, 2013]. Initial calibration of the pattern is made with reference to a beryl-quartz standard contained in one of the cells on the CheMin sample wheel. Tolerance variations in the machining of the sample cell assemblies cause individual cells to be offset from their ideal diffraction position by up to ±80 μm relative to an ideal sample cell-to-CCD distance of 18.5302 mm. To counter this positioning offset and the resulting shift in 2-theta peak positions, an internal calibration method was developed based on the refined cell parameters of plagioclase (present as a major phase in all but one of the samples measured by CheMin) [*Morrison et al.*, 2017]. The sample cell offset calibration method was developed after the Rocknest data were published [*Bish et al.*, 2013; *Blake et al.*, 2013]. Newly revised mineral abundances and crystal chemistry for Rocknest data in addition to the data for Gobabeb are presented here.

Rietveld refinements of the calibrated patterns are used to calculate mineral abundances and unit-cell parameters of the major crystalline phases. Individual mineral chemistries are determined from refined unit cell parameters by comparison to relationships between unit cell parameters and compositions of published mineral data [*Lafuente et al.*, 2015; *Morrison et al.*, 2017]. The abundance of the amorphous component was estimated from FULLPAT analyses of the diffraction pattern using natural and synthetic X-ray amorphous phases as standards [*Chipera and Bish*, 2013]. The chemical composition of the amorphous component was estimated from mass balance calculations using the APXS-determined bulk composition of the $<$150 μm sieved fraction and the quantity and composition of the crystalline components determined from Rietveld refinement [*Morris et al.*, 2016; *Morrison et al.*, 2017].

We performed a second analysis of the Gobabeb sample using the more rigorous direct cell vibration. Significant sample loss occurred during the analysis, indicated by dramatic changes in diffraction intensities with a commensurate increase in diffraction intensity from the Mylar cell window, and resulted in a measurement that was no longer representative of the bulk $<$150 μm sample fraction. Prelaunch laboratory tests of sample vibration in CheMin cells showed that coarser-grained materials couple more strongly to cell vibration than fine-grained materials and as a result are more readily ejected from the cell. By quantifying changes in phase abundance relative to the increase in Mylar we can estimate the relative grain size of phases identified in the Gobabeb diffraction patterns.

A distinct analysis approach was used to determine the relative abundances of Mylar, the crystalline fraction, and the X-ray amorphous component in the indirect and direct vibration patterns. The diffraction pattern of the empty 7A Mylar cell, acquired on sol 90, was incorporated as a unique phase in the Rietveld model. The scale factor of the Mylar diffraction pattern was refined along with the parameters from the crystalline phases. A reference intensity ratio was assigned to the Mylar pattern to convert the modeled intensity to an estimated abundance. Amorphous phases were modeled as broad humps. The total amorphous contribution was determined by dividing the integrated intensity of the amorphous humps by the integrated intensity of whole Rietveld model (i.e., crystalline + amorphous + Mylar). Results obtained from these Mylar-based refinement models are reported for the following reasons: (1) these trends allow us to estimate relative

Table 1. Gobabeb and Rocknest Mineral Abundances From Rietveld Refinement and FULLPAT Analyses of CheMin XRD Data[a]

	Gobabeb		Rocknest	
	Crystalline	Crystalline + Amorphous	Crystalline	Crystalline + Amorphous
Plagioclase	36.5(8)	23.7(8)	40.7(5)	26.3(7)
Olivine	25.8(4)	16.8(6)	20.5(4)	13.3(4)
Augite	22.0(4)	14.3(6)	18.1(13)	11.7(9)
Pigeonite	10.6(4)	6.9(6)	12.3(12)	8.0(8)
Magnetite	2.1(2)	1.4(2)	2.8(5)	1.8(3)
Anhydrite	1.3(1)[b]	0.8(1)	1.4(3)[b]	0.9(2)
Hematite	0.9(1)[b]	0.6(2)	1.6(1)[b]	1.0(1)
Quartz	0.8(1)[b]	0.5(1)	1.3(3)[b]	0.8(2)
Ilmenite	–	–	1.3(5)[b]	0.9(3)
Amorphous	–	35(15)[c]	–	35(15)

[a]Abundances in wt %; uncertainties reported as 1σ.
[b]At or below the detection limit.
[c]FULLPAT analysis; APXS-constrained value is ~42%.

mineral grain sizes and (2) the direct vibration data increased the relative abundance of some minor phases and thus validated their presence in the Gobabeb eolian sample.

3. Results

3.1. Gobabeb Crystalline Component

Gobabeb is dominated by basaltic minerals and X-ray amorphous phases. Plagioclase (36.5 wt %), Fo56 olivine (25.8 wt %), and two types of Ca-Mg-Fe pyroxene (32.6 wt %) comprise most of the mass of the crystalline phases; minor minerals include magnetite (2.1 wt %), quartz (1.3 wt %), hematite (0.9 wt %), and anhydrite (0.8 wt %) (Table 1). The mineral chemistry of major phases is estimated from refined unit-cell parameters of the indirectly vibrated sample (Tables 2 and 3) [*Morrison et al.*, 2017]. The average compositions calculated for plagioclase and olivine are $(Ca_{0.63(5)}Na_{0.37})(Al_{1.63}Si_{2.37})O_8$ and $(Mg_{1.11(6)}Fe_{0.89})Si_2O_4$, respectively. Two pyroxene phases were identified: augite, a high-Ca, monoclinic phase with composition $(Mg_{1.03(15)}Ca_{0.81(11)}Fe_{0.16(19)})Si_2O_6$, and pigeonite, a low-Ca, monoclinic phase with composition $(Mg_{1.03(23)}Fe_{0.79(25)}Ca_{0.18(11)})Si_2O_6$. The diffraction peaks defining augite and pigeonite overlap in several regions, making it difficult to model the abundance and unit-cell parameters accurately for the individual pyroxene phases. As a result, estimated abundance and mineral chemistry are less certain for these phases than for plagioclase and olivine.

Table 2. Unit-Cell Parameters for Major Gobabeb and Rocknest Minerals From Rietveld Refinements of CheMin XRD Data[a]

	a (Å)	b (Å)	c (Å)	α (°)	β (°)	γ (°)	V (Å^3)
			Gobabeb				
Plagioclase	8.181(7)	12.868(7)	7.107(6)	93.49(5)	116.19(4)	90.06(3)	669.8(8)
Olivine	4.785(3)	10.327(3)	6.033(4)	90	90	90	298.1(3)
Augite	9.785(15)	8.922(13)	5.276(13)	90	106.45(9)	90	441.8(14)
Pigeonite	9.675(22)	8.941(27)	5.254(29)	90	108.69(14)	90	430.6(25)
			Rocknest				
Plagioclase	8.168(6)	12.863(6)	7.108(4)	93.46(5)	116.22(3)	90.12(3)	668.4(5)
Olivine	4.785(3)	10.318(4)	6.025(3)	90	90	90	297.5(2)
Augite	9.767(22)	8.924(13)	5.263(11)	90	106.47(21)	90	440.0(15)
Pigeonite	9.651(15)	8.942(18)	5.235(21)	90	108.35(8)	90	428.9(22)

[a]Uncertainties reported as 1σ.

Table 3. Chemical Compositions of Major Gobabeb and Rocknest Minerals Determined From Crystal Chemical Analysis of Refined Unit-Cell Parameters[a]

Gobabeb	
Plagioclase	$(Ca_{0.63(5)}Na_{0.37})(Al_{1.63}Si_{2.37})O_8$
Olivine	$(Mg_{1.11(6)}Fe_{0.89})SiO_4$
Augite	$(Mg_{1.03(15)}Ca_{0.81(11)}Fe_{0.16(19)})Si_2O_6$
Pigeonite	$(Mg_{1.03(23)}Fe_{0.79(25)}Ca_{0.18(11)})Si_2O_6$
Revised Rocknest	
Plagioclase	$(Ca_{0.50(4)}Na_{0.50})(Al_{1.50}Si_{2.50})O_8$
Olivine	$(Mg_{1.15(5)}Fe_{0.85})SiO_4$
Augite	$(Mg_{1.01(15)}Ca_{0.80(11)}Fe_{0.19(19)})Si_2O_6$
Pigeonite	$(Mg_{1.02(16)}Fe_{0.88(18)}Ca_{0.10(9)})Si_2O_6$
Original Rocknest[b]	
Plagioclase	$(Ca_{0.57(13)}Na_{0.43})(Al_{1.57}Si_{2.43})O_8$
Olivine	$(Mg_{1.24(6)}Fe_{0.76})SiO_4$
Augite	$(Mg_{0.88(10)}Ca_{0.75(4)}Fe_{0.37(12)})Si_2O_6$
Pigeonite	$(Mg_{1.13(12)}Fe_{0.68(12)}Ca_{0.19(5)})Si_2O_6$

[a]Uncertainties reported as 1σ.
[b]Compositions initially published in *Bish et al.* [2013].

3.2. Gobabeb Amorphous Component

Mass balance calculations derived from APXS chemical data and CheMin mineral abundances and crystal chemistry provide an estimate of the composition of the X-ray amorphous component in Gobabeb. FULLPAT modeling of the diffraction data suggest that ~35(15) wt % of the Gobabeb sample is amorphous material, which is modeled as a mixture of basaltic and rhyolitic glasses. The calculated composition of the amorphous material (Table 4) is based on a minimum of ~42 wt % amorphous phases. This lower limit is constrained by the fact that when the combined crystalline and amorphous compositions are compared to the APXS chemistry, the least abundant oxide, in this case MgO, must be greater than or equal to zero in the calculated amorphous component. Given an ~42 wt % amorphous minimum, the major constituents of the calculated amorphous component include ~50 wt % SiO_2, ~20 wt % FeO_T (Fe^{2+} plus Fe^{3+}), ~8 wt % Al_2O_3, and ~7 wt % SO_3.

3.3. Indirect Versus Direct Vibration of the Gobabeb Sample

Indirect and direct cell vibrations produced distinctly different diffraction patterns. Most evident are considerable variations in peak intensities that can be ascribed to changes in mineral abundances and an increase in the diffraction contribution from the Mylar cell window (Figure 6). For both the indirect and direct patterns, the relative abundance of each crystalline phase, along with estimates of the amorphous component and the Mylar contribution, was determined using the distinct, Mylar-based refinement model (see section 2.2) and are shown in Table 5. It is important to note that although the relative proportion of crystalline phases

Table 4. APXS <150 μm Gobabeb Composition and Calculated Compositions of Crystalline and Amorphous Components From CheMin-Derived Mineral Chemistry[a,b]

	<150 μm[c]	Crystalline[d]	Amorphous[d]	Crystalline[e]	Amorphous[e]
SiO_2	47.88	27.34	20.54	46.73	49.53
TiO_2	0.88	0.00	0.88	0.00	2.12
Al_2O_3	9.78	6.52	3.26	11.15	7.86
FeO_T	17.91	9.69	8.22	16.56	19.82
MnO	0.37	0.00	0.37	0.00	0.89
MgO	7.57	7.57	0.00	12.94	0.00
CaO	7.30	6.03	1.27	10.31	3.06
Na_2O	2.75	0.90	1.85	1.54	4.46
K_2O	0.49	0.00	0.49	0.00	1.18
P_2O_5	0.79	0.00	0.79	0.00	1.91
Cr_2O_3	0.39	0.00	0.39	0.00	0.94
Cl	0.50	0.00	0.50	0.00	1.21
SO_3	3.36	0.45	2.91	0.77	7.02
Total	99.97	58.50	41.47	100.00	100.00

[a]Oxides and Cl are reported in wt %.
[b]Method described in *Morris et al.* [2016] and *Morrison et al.* [2017].
[c]APXS analysis of Gobabeb, postsieve, <150 μm sand fraction dump pile [*O'Connell-Cooper et al.*, 2017].
[d]Proportion of the bulk sample; crystalline and amorphous sum to 100%.
[e]Components normalized to 100%.

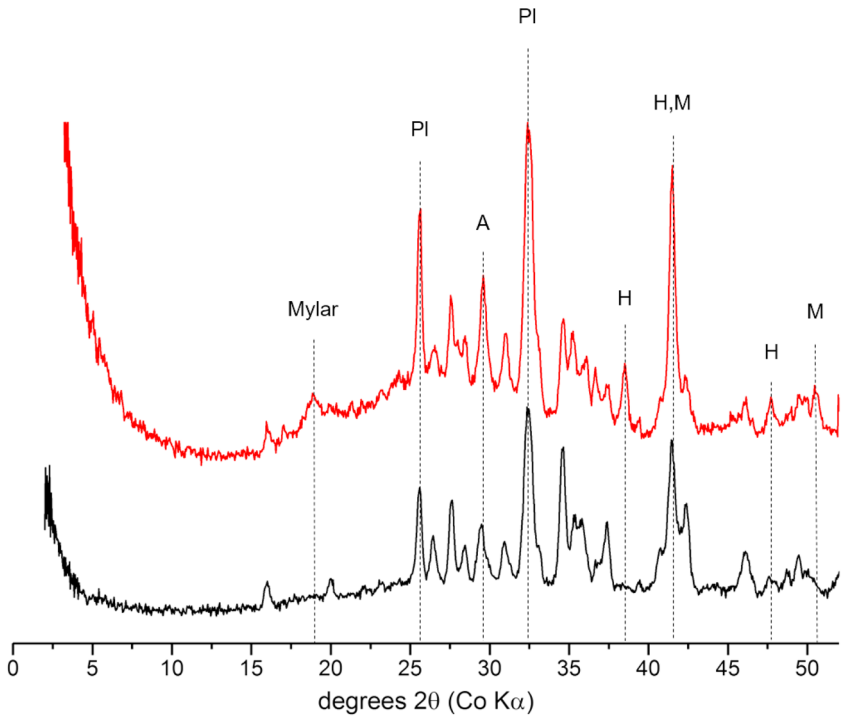

Figure 6. Gobabeb diffraction patterns resulting from indirect vibration (black) and direct vibration (red). Normalized to equal analysis times. Labeled peaks correspond to the following minerals: Pl = plagioclase, A = anhydrite, H = hematite, and M = magnetite.

determined from the Mylar-based model are within 1σ of the phase abundances reported in Table 1 (2σ for pigeonite, hematite, and quartz), the values in Table 5 are reported strictly to illustrate the relative changes between the indirect and direct patterns.

Coarse- and fine-grained materials respond differently to vibrations in the CheMin sample cell, as described earlier. Based on vibration experiments, we assume that the material remaining in the Gobabeb cell during the direct vibration analysis contains a higher abundance of fine-grained material, because a significant portion of the sample, likely the coarser fraction, was lost from the cell. We observe clear decreases in olivine and augite and increases in hematite, anhydrite, and the amorphous component (Table 5). Comparing the two diffraction data sets, we calculated direct:indirect phase abundance ratios in order to explore the statistical significance of the observed abundance differences. Each phase's direct:indirect ratio was normalized to the Mylar direct:indirect ratio. Mylar is regarded as the constant phase between analyses as the volume of Mylar exposed to the X-ray beam is the same in each measurement.

Table 5. Comparison of Gobabeb Phase Abundances for Indirect and Direct Vibration Modes Obtained From a Mylar-based Rietveld Refinement Model of CheMin XRD Patterns[a]

	Indirect Vibration[b]	Direct Vibration[b]
Plagioclase	18.0(3)	16.9(4)
Olivine	12.9(3)	3.7(3)
Augite	11.3(4)	3.1(4)
Pigeonite	4.4(4)	2.9(4)
Magnetite	1.2(1)	2.7(2)
Hematite	0.7(1)[c]	2.1(1)
Anhydrite	0.7(1)[c]	2.0(1)
Quartz	0.6(1)[c]	1.1(2)
Amorphous	49.0	63.3
Mylar	1.2(2)	2.2(2)

[a]Abundances in wt %; uncertainties reported as 1σ.
[b]Vibration modes are described in the text and in [*Downs and MSL Team*, 2015].
[c]At or near detection limit.

The ratios show that there is a clear decrease in augite, olivine, pigeonite, and plagioclase abundances and an increase in hematite and anhydrite (Figure 7). The amorphous component decreased relative to Mylar,

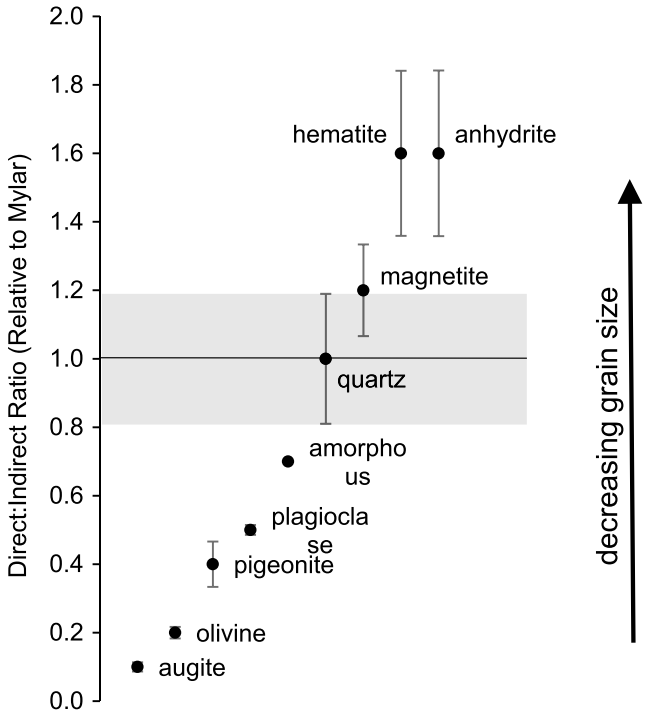

Figure 7. Measured phase abundance ratios relative to Mylar cell window diffraction intensity (Mylar = one) for Gobabeb, analyzed via direct and indirect cell vibration. Ratios less than one indicate a relative decrease of the phase whereas ratios greater than one indicate a relative increase in abundance. In unconsolidated materials such as Gobabeb, coarse-grained phases are preferentially ejected from the sample cell relative to fine-grained phases at the higher vibration amplitudes. Uncertainties are represented by bars for each mineral phase and as the shaded area for Mylar.

although the significance cannot be determined because errors for the amorphous abundance are undefined in the Mylar-based refinement model. Thus, augite, olivine, pigeonite, and plagioclase represent the larger grains while hematite and anhydrite are smaller. Compositional trends in the APXS-analyzed size fractions also show enrichment in olivine and pyroxene in the coarse fraction [*Ehlmann et al.*, 2017], consistent with the trend observed in Figure 7. All these minerals, except the softer anhydrite, have similar hardness (5.5–7.0 on the Mohs scale) so it is likely that they would wear at similar rates during dune movements. The Gobabeb indirect and direct vibration experiments clearly show that grain motion directly influences the absolute accuracy of reported mineral abundances.

3.4. Rocknest Mineralogy

The revised Rocknest mineralogy shows significant improvement in major phase chemistries calculated from measured unit-cell parameters. Mineral abundances and crystal chemistry derived from the newly calibrated Rocknest diffraction pattern are shown in Tables 1–3. Rietveld refinements of the pattern produced major mineral abundances consistent with those originally published in *Bish et al.* [2013] and *Blake et al.* [2013], with the exception of K-feldspar which was not identified in the newly calibrated pattern. Phase compositions derived from refined cell parameter measurements are significantly different from those originally published. The cell offset correction improved the accuracies of refined unit cell parameters and, in turn, the derived mineral compositions. These improvements are most evident in the calculated plagioclase chemistry which shows a threefold error reduction. The plagioclase composition is estimated to be $(Ca_{0.50(4)}Na_{0.50})(Al_{1.50}Si_{2.50})O_8$, and the olivine composition is $(Mg_{1.15(5)}Fe_{0.85})SiO_4$. Augite and pigeonite compositions are estimated as $(Mg_{1.01(15)}Ca_{0.80(11)}Fe_{0.19(19)})Si_2O_6$ and $(Mg_{1.02(16)}Fe_{0.88(18)}Ca_{0.10(9)})Si_2O_6$, respectively. We consider the values reported here to be more accurate than those reported in *Bish et al.* [2013] and *Blake et al.* [2013].

4. Discussion

4.1. Gobabeb Mineralogy

Curiosity's analysis of material from the Bagnold Dune Field presents a rare opportunity to provide mineralogical ground truth for orbital observations. Surface and ground-based mineralogies are especially comparable in the Bagnold Dune Field due to negligible amounts of fine-grained dust cover that typically dominates the orbital signature of much of the Martian surface but is diminished in the dunes due to active sediment transport. The low dust content at Gobabeb is supported by APXS analyses of these sands showing low concentrations of S, Cl, and Zn, elements associated with Martian dust [*O'Connell-Cooper et al.*, 2017]. Using deconvolution models of thermal emission spectra collected by the Thermal Emission Spectrometer (TES) on Mars Global Surveyor, *Rogers and Bandfield* [2009] calculated volume abundances for Bagnold

Table 6. APXS Chemical Compositions of Rocknest and Gobabeb Bulk and <150 μm Fractions[a,b]

	Rocknest	Gobabeb	Gobabeb
	Bulk[c]	Bulk[c]	<150 μm
SiO_2	42.97	48.15	47.88
TiO_2	1.19	0.84	0.88
Al_2O_3	9.37	10.01	9.78
FeO_T	19.18	17.50	17.91
MnO	0.42	0.37	0.37
MgO	8.69	8.36	7.57
CaO	7.26	7.20	7.30
Na_2O	2.70	2.67	2.75
K_2O	0.49	0.48	0.49
P_2O_5	0.95	0.75	0.79
Cr_2O_3	0.49	0.32	0.39
Cl	0.69	0.50	0.50
SO_3	5.47	2.82	3.36
Total	99.87	99.97	99.97

[a][*Blake et al.*, 2013; *O'Connell-Cooper et al.*, 2017].
[b]Compositions in wt %.
[c]Bulk analyses represent measurements of disturbed soil.

dune phases. They determined that the dune field contained 20(5)% feldspar, 30(9)% pyroxene, 15(4)% olivine, 19(5)% high-silica phases (including possible silica glass, opal, zeolite, and phyllosilicate), and 12(2)% sulfate and 4% other phases. CheMin-estimated crystalline plus amorphous abundances (Table 1) and the TES-derived phase distributions show that feldspar (20% TES, 24 wt % CheMin) and olivine (15% TES, ~17 wt % CheMin) are consistent with one another but lower amounts of pyroxene (30% TES, ~21 wt % CheMin) are observed in the CheMin mineralogy. Furthermore, the CheMin-derived composition of the olivine, Fo56(3), is nearly identical to that calculated from TES analyses (Fo55(5) [*Lane and Christensen*, 2013]). These TES data represent a bulk sand analysis, whereas CheMin data reflect the <150 μm sand fraction acquired at a single sample site. Normative mineralogy calculations derived from APXS analyses of the bulk sand and the <150 μm fraction yield estimated mineral abundances within error of one another (Tables 6 and 7). These normative data validate CheMin and TES mineralogy comparisons, even though the CheMin analyzed sample was a subset of the TES-measured bulk eolian deposit.

CheMin data also provide definitive mineralogical ground truth for VNIR spectra from the Compact Reconnaissance Imaging Spectrometer for Mars (CRISM) instrument on Mars Reconnaissance Orbiter. CRISM spectra of other barchan dunes in Gale crater, similar to the Namib dune from which Gobabeb was sampled, imply that the sands contain significant amounts of both the more abundant olivine and the less abundant high-Ca pyroxene [*Seelos et al.*, 2014], consistent with the CheMin results which show ~26 wt % olivine and 22 wt % augite in the crystalline fraction. A targeted study by *Lapotre et al.* [2017] quantitatively estimated the abundances of olivine, plagioclase, pyroxene, magnetite, and volcanic glass at the Namib dune based on radiative transfer theory modeling of CRISM data. Their predicted 95% confidence intervals on phase abundances contain the CheMin-determined mineralogy from Gobabeb [*Lapotre et al.*, 2017].

CRISM studies of the Bagnold Dune Field are important for revealing mineralogical trends that may indicate potential parent rocks. Regional CRISM studies of Gale and surrounding craters show that olivine-bearing units, some with high-Ca pyroxene, are present throughout the region and most notably in the upper wall rocks of Gale crater's rim; these could be source materials for the Bagnold Dune sediments [*Ehlmann and Buz*, 2015]. The compositions of Gobabeb's major minerals add further constraints to the origins of the sediment. Figure 8 shows the CheMin-derived chemical compositions of pyroxenes (augite and pigeonite) and olivine in the Gobabeb and Rocknest samples on a standard "pyroxene quadrilateral" diagram. The olivine and pigeonite

Table 7. CIPW Normative Mineralogy Calculated From APXS Analyses of the Bulk and <150 μm Gobabeb Sand Fraction Chemistry[a,b]

	Normative Mineralogy	
	Bulk	<150 μm
Plagioclase	36.50	36.16
Hypersthene	29.45	29.21
Diopside	12.45	13.14
Olivine	8.85	7.75
Orthoclase	2.84	2.90
Magnetite	2.54	2.60
Apatite	1.74	1.83
Ilmenite	1.60	1.67
Total	95.97	95.26

[a]Abundances in wt %.
[b]APXS chemistry in Table 6.

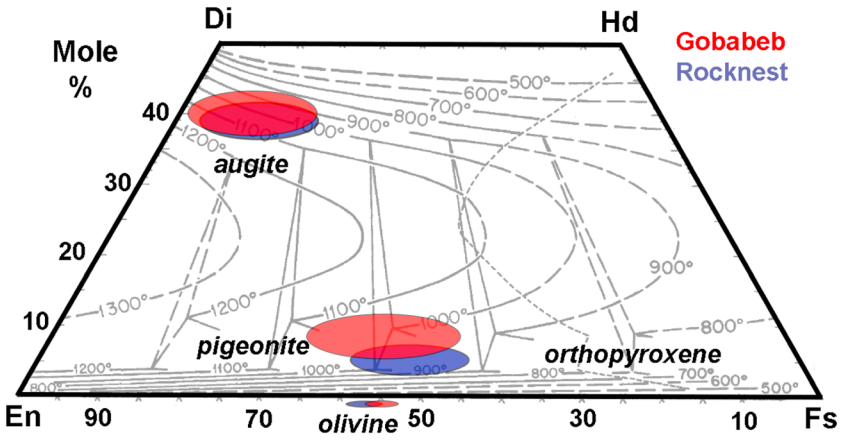

Figure 8. Inferred compositions of olivine and pyroxenes of Gobabeb and revised Rocknest samples shown in the standard pyroxene quadrilateral in mole percents of the components enstatite, En ($MgSiO_3$); ferrosilite, Fs ($FeSiO_3$), and wollastonite ($CaSiO_3$). Other pyroxene endmembers are diopside, Di ($CaMgSi_2O_6$), and hedenbergite Hd ($CaFeSi_2O_6$). The light background lines are the liquidus equilibria positions and tie-lines for pyroxenes [*Lindsley*, 1983]. The molar Mg/(Mg + Fe) ratio for olivine and pigeonite are similar, but augite is distinctly more magnesian in both the Gobabeb and Rocknest sands. This difference suggests that olivine and pigeonite formed in different environments from augite.

in Gobabeb have similar molar values while the augite has distinctly higher Mg/(Mg + Fe) than either olivine or pigeonite. This difference suggests several possible formation scenarios. First, it is possible that the olivine and pigeonite came from the same source rock, while the augite came from a different rock [*Lindsley*, 1983]. For example, the olivine and pigeonite could have come from one basaltic source (e.g., material with a compositions similar to a basaltic or lherzolitic shergottite meteorite [*McSween and Treiman*, 1998]), while the augite could have come from a different basaltic source (e.g., like the nakhlite or NWA 8159 meteorites [*Treiman*, 2005; *Agee et al.*, 2014]).

A second interpretation is that the olivine and pyroxene could represent chemically zoned minerals from a single igneous rock. For example, a basaltic rock that first crystallized abundant magnesian augite and later crystallized ferroan pigeonite and olivine without augite could yield average mineral compositions like those of Gobabeb (Figure 8). No known Martian meteorite basalts have crystallization sequences like this (augite crystallizing early but not later) [*McSween and Treiman*, 1998; *Treiman*, 2005; *Agee et al.*, 2014; *Udry et al.*, 2014; *Santos et al.*, 2015], but the meteorite collection certainly does not include every possible Martian basaltic rock. Such mineral chemical zoning or variation could be apparent in X-ray diffraction patterns as broadened diffraction peaks. However, CheMin's relatively low resolution, ~0.3° 2θ, makes it difficult to determine whether the augite diffraction peaks for Gobabeb are broadened.

Another possibility is that the pyroxenes and olivines could represent a magma similar to those that formed the nakhlite Martian meteorites [*Treiman*, 2005] that had partially equilibrated on cooling. Such a magma would first crystallize magnesian augite and olivine and produce ferroan, low-Ca pyroxene only toward the end of crystallization. If this end-stage crystallization were relatively slow, the olivine could have equilibrated with the late magma, yielding olivine with the same low Mg/(Mg + Fe) as the low-Ca pyroxene. Such a pattern is like that of the Lafayette nakhlite meteorite [*Treiman*, 2005], although the minerals in Lafayette itself are overall more ferroan than those in Gobabeb and Rocknest.

In addition to the crystalline phases, the Gobabeb eolian sample contains a calculated ~42 wt % minimum abundance of amorphous materials based on APXS constraints. The identity of specific amorphous phases cannot be determined from the diffraction pattern alone, because many different X-ray amorphous materials produce similar broad scattering profiles [e.g., *Morris et al.*, 2015]. However, the chemical composition of the amorphous component can suggest the nature of its potential constituents. The calculated amorphous composition in Table 4 shows that nearly 90 wt % is composed of SiO_2, FeO_T, Al_2O_3, SO_3, and Na_2O. It is important to note that the calculated amorphous composition is MgO-deficient. This does not necessarily mean that Mg is absent from the amorphous component; if amorphous Mg-bearing phases are indeed present, the amorphous fraction would have to exceed the minimum calculated value of ~42 wt %. Given this constraint, the

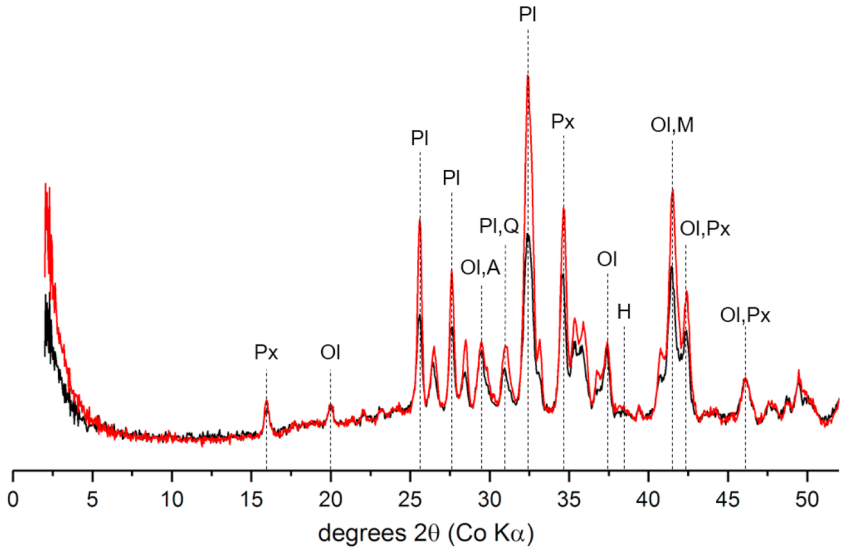

Figure 9. Rocknest (black) and Gobabeb (red) diffraction patterns. Patterns are normalized to reflect equal analysis times. Labeled peaks correspond to the following minerals: Pl = plagioclase, Px = pyroxene, Ol = olivine, A = anhydrite, Q = quartz, H = hematite, and M = magnetite.

amount of SiO_2, ~50 wt %, cannot be modeled with a single basaltic phase (i.e., basaltic glass). Instead, a combination of phases is proposed. Maskelynite, allophane, and amorphous silica (e.g., opal-A and opal-CT) are all geochemically viable phases that have a high silica content; all of these are not only SiO_2-rich but also low in Mg. CheMin analyses of the nearby Murray formation detected opal-CT which may indicate local contributions to the Gobabeb sediment [*Rampe et al.*, 2017]. The detection of high concentrations of tridymite in one Murray mudstone provides evidence for silicic volcanism and suggests a source close to Gale crater, possibly the crater rim where studies have provided evidence for evolved igneous lithologies that could act as a contributing source to the Bagnold sands [*Sautter et al.*, 2015; *Morris et al.*, 2016].

The remaining amorphous component is comprised mainly of FeO_T, Al_2O_3, SO_3, and Na_2O. A majority of the amorphous FeO_T is likely attributed to nanophase iron oxides, which are common components in Martian dust and soils [*Morris et al.*, 2006a; *Ming et al.*, 2008]. Al_2O_3 and SO_3 each comprise ~7 wt % of the amorphous component. Maskelynite, allophane, and/or amorphous Al-sulfates are possible Al-bearing phases. The low dust component in the Gobabeb dune implies that the SO_3 is likely not attributed entirely to dust and indicates the probable presence of amorphous sulfates. Additional phases have been suggested based on results from the Evolved Gas Analyzer (EGA) of the Sample Analysis at Mars (SAM) instrument. EGA data suggest the presence of carbonate, Mg-sulfate phases, and chlorate and/or perchlorate species [*Sutter et al.*, 2017]. If present, these phases are either amorphous or, if crystalline, below the CheMin detection limit (~1 wt % [*Blake et al.*, 2012]) and, consequently, are included in the amorphous component of the chemical composition calculation.

4.2. Rocknest Comparison

Mineralogical comparisons of Rocknest and Gobabeb are important for predicting whether the sediments originate from the same parent material and how eolian activity affects mineral distributions. The Rocknest and Gobabeb diffraction patterns show remarkable similarities in peak positions and relative intensities (Figure 9). Overall intensity variations between the two patterns are likely due to grain motion effects, with Rocknest exhibiting higher intensities due to more homogenous grain movement compared to Gobabeb. The fine-grained materials in Rocknest coat larger grains (Figure 4b) and likely cause the sample to move cohesively in the cell. Like Gobabeb, over 90% of the crystalline material in Rocknest is composed of plagioclase, olivine, and pyroxene, with minor phases that include magnetite, anhydrite, hematite, and quartz, as initially reported in *Bish et al.* [2013]. The inferred compositions of mafic minerals in Rocknest and Gobabeb are strikingly similar (Table 3). Olivine, augite, and pigeonite share nearly identical chemical compositions in the respective samples; as with the Gobabeb pyroxenes, the augite and pigeonite in Rocknest are

Table 8. Comparison of Calculated Compositions of Crystalline and Amorphous Components in Rocknest and Gobabeb[a]

	Crystalline		Amorphous	
	Rocknest	Gobabeb	Rocknest	Gobabeb
SiO_2	47.62	46.73	34.58	49.53
TiO_2	0.68	0.00	2.12	2.12
Al_2O_3	11.52	11.15	5.45	7.86
FeO_T	16.95	16.56	23.27	19.82
MnO	0.00	0.00	1.20	0.89
MgO	11.32	12.94	4.05	0.00
CaO	8.76	10.31	4.45	3.06
Na_2O	2.33	1.54	3.38	4.46
K_2O	0.00	0.00	1.39	1.18
P_2O_5	0.00	0.00	2.70	1.91
Cr_2O_3	0.00	0.00	1.39	0.94
Cl	0.00	0.00	2.96	1.21
SO_3	0.82	0.77	14.04	7.02
Total	100.00	100.00	100.00	100.00

[a]Oxides and Cl are reported in wt %.

not in equilibrium with one another, as evidenced by olivine and pigeonite having similar molar Mg/(Mg + Fe), while the augite is significantly more magnesian (Figure 8). The Gobabeb plagioclase is distinctly more calcic than that in Rocknest (An63(5) versus An50(4), respectively). Even though the olivine and pyroxene chemistries are similar, one explanation for the plagioclase variation is that Rocknest and Gobabeb represent two distinct primary mineral suites, each derived from different parent basalts.

Chemical differences between Gobabeb and Rocknest highlight the different eolian environments of these sands. The present-day inactivity of the Rocknest sand shadow allowed significant proportions of wind-blown dust to accumulate, as indicated by higher SO_3 content of the bulk sand (5.47 wt % in Rocknest versus 2.82 wt % in bulk Gobabeb; Table 6). Additionally, the increased FeO_T abundance in the Rocknest amorphous component (23.27 wt % versus 19.82 wt % in Gobabeb; Table 8) reflects a higher proportion of nanophase iron oxide (npOx) phases compared to the more active Gobabeb deposit. In the calculated amorphous component, Gobabeb has ~20 wt % more SiO_2 than Rocknest, a substantial difference that is not well understood (Table 8). However, nearby mudstones from the Murray formation and alteration zones in the Stimson formation contain significant amounts of amorphous silica and could be a local source of SiO_2 in Gobabeb [*Morris et al.*, 2016; *Rampe et al.*, 2017; *Yen et al.*, 2017].

4.3. Gale, Meridiani, and Gusev Eolian Deposits

Definitive mineralogy and phase chemistry of sediments in Gale crater have added new and unique data for assessing young and ancient eolian deposits in Gale and characterizing potential sediment sources for unconsolidated materials across Mars. Within Gale crater, Curiosity investigated the Stimson formation, described as ancient, lithified eolian dunes [*Banham et al.*, 2016]. This formation, adjacent to the Bagnold Dunes, is a cross-bedded sandstone unit that includes significant alteration zones. Mineralogical comparisons between the ancient, unaltered Stimson targets Big Sky and Okoruso and young, Rocknest and Gobabeb eolian samples show comparable plagioclase and pyroxene abundances; olivine is not identified in Big Sky and is present at ~2 wt % in Okoruso, a depletion attributed to olivine transformation to magnetite and hematite during diagenesis [*Yen et al.*, 2017]. APXS analyses of Big Sky and Okoruso show chemical compositions similar to present-day unconsolidated materials in Gale, Meridiani, and Gusev, indicating a common crustal composition between ancient and young basaltic sediments [*Yen et al.*, 2017].

Mineralogical and geochemical comparisons between modern and ancient eolian materials (for example, comparison of Rocknest and Gobabeb soils to the Stimson eolian sandstone) provide a powerful means to relate modern and ancient eolian activity, sediment provenance, and diagenetic modification. Prior to CheMin and MSL, the combination of APXS and Mössbauer spectroscopy on the MERs led to a classification of rocks and soils based primarily on the distribution of Fe among Fe-bearing phases and elemental enrichments and/or depletions compared to an average rock class [*Ming et al.*, 2008]. These data provided estimates of the abundance and chemistry of Fe-bearing phases but relied on normative calculations to evaluate the collective mineralogy of both Fe and non-Fe bearing materials. Curiosity's combination of APXS and CheMin offers a uniquely synergistic data set, allowing a more thorough interpretation of Rocknest, Gobabeb, and Stimson eolian materials, as well as a renewed interpretation of data sets obtained in earlier missions. CheMin data provide definitive detections of all crystalline phases present at

Table 9. APXS Compositions of Average Basaltic Soils in Gale Crater, Meridiani Planum, and Gusev Crater Along With Select Individual Analyses Normalized to 100% Totals[a]

	Gale			Meridiani	Gusev	
	Average[b]	Rocknest	Gobabeb	Average[c]	Average[c]	El Dorado[d]
SiO_2	43.16	43.02	47.90	46.14	46.32	47.55
TiO_2	1.05	1.19	0.88	1.03	0.87	0.73
Al_2O_3	9.16	9.38	9.78	9.39	10.14	10.91
FeO_T	19.33	19.20	17.92	18.17	16.04	15.82
MnO	0.42	0.42	0.37	0.37	0.32	0.31
MgO	8.60	8.70	7.57	7.42	8.61	10.01
CaO	7.08	7.27	7.30	6.95	6.35	6.31
Na_2O	2.72	2.70	2.75	2.23	3.01	3.20
K_2O	0.50	0.49	0.49	0.49	0.44	0.37
P_2O_5	0.92	0.95	0.79	0.85	0.82	0.75
Cr_2O_3	0.46	0.49	0.39	0.40	0.35	0.34
Cl	0.77	0.69	0.50	0.66	0.72	0.40
SO_3	5.83	5.48	3.36	5.91	6.01	3.30
Ni	518	456	504	469	465	684
Zn	323	327	190	309	285	145
Br	43	34	37	81	52	29

[a]Oxides and Cl are reported in wt % and normalized to 100%; Ni, Zn, and Br are reported as ppm.
[b]*O'Connell-Cooper et al.* [2017].
[c]Average composition of basaltic soils listed in *Yen et al.* [2006].
[d]Edgar scuff analysis [*Ming et al.*, 2008].

$\geq$ ~1 wt %, and when combined with APXS data provide estimates of the composition of both crystalline and amorphous components.

APXS analyses of basaltic soils in Gale, Meridiani, and Gusev have similar chemical compositions (Table 9). Meridiani and Gusev averages are within 1σ of each other, and the average from Gale is within 2σ of those from MER average soils. The olivine mineralogy for young Gale sediments (Fo58(1) for Rocknest and Fo56(3) for Gobabeb) is similar to the Gusev olivine composition (Fo60) modeled from Mössbauer data, and falls within the range of olivine in Shergottite meteorites (Fo53 to Fo76) [*Morris et al.*, 2004; *Bridges and Warren*, 2006]. In addition to Fe-bearing phases identified in Mössbauer-analyzed soils, non-Fe bearing minerals were proposed based on models of thermal emission spectra acquired by the MER's Miniature Thermal Emission Spectrometer (Mini-TES). Mini-TES soil analyses from Opportunity's first 350 sols were analyzed to produce a dust-free, basaltic sand end-member representative of the average basaltic sand spectrum observed at Meridiani Planum [*Glotch and Bandfield*, 2006]. In a study by *Rogers and Aharonson* [2008], the end-member spectrum was modeled to derive mineralogical abundances representative of the Meridiani basaltic sands. Results from various phase combinations show that these basaltic sands are composed of ~10–15% olivine, pyroxene abundances nearly twice that of olivine, ~10% sulfate, and ~10–20% amorphous silica phases (reported as volume %) [*Rogers and Aharonson*, 2008]. Models also determined that pigeonite or an iron-rich pyroxene must be present with orthopyroxene and/or a high-Ca pyroxene to match the Fe_{olv} to Fe_{pyx} ratio in Meridiani low-sulfur soils [*Morris et al.*, 2006b; *Rogers and Aharonson*, 2008]. Phase abundances averaged from the five closest-fitting spectral models show similar feldspar and olivine abundances but higher abundances of pyroxene and sulfur compared Gobabeb. Feldspar and olivine average ~24 vol% (~21 wt %) and ~14 vol% (~18 wt %) for the Meridiani end-member basaltic sand, similar to Gobabeb with ~24 wt % feldspar and 18 wt % olivine. Pyroxene abundances at Gobabeb are not twice that of olivine as observed at Meridiani but given the high-olivine nature of the Namib dune, one-to-one mineralogical comparisons of low-dust MER soils and Gobabeb may be strongly affected by mineralogical sorting observed in the Bagnold Dune Field.

Of the low-dust soils analyzed by the MERs, Spirit's investigation of the El Dorado ripple field in Gusev crater shares many similarities to the sediments observed in the Bagnold dunes and is an excellent comparative sample to Gobabeb. In situ spectral measurements of El Dorado revealed two fractions, a coarse-grained top layer with a spectral pattern consistent with >60 μm olivine and a finer-grained fraction with a higher abundance of low-Ca pyroxene than observed in the coarse sand [*Sullivan et al.*, 2008]. Multispectral imaging and chemical data of Gobabeb size fractions show a similar trend, with more olivine in the coarse fraction

(>150 μm) compared to the finer (<150 μm) fraction [*Ehlmann et al.*, 2017; *Johnson et al.*, 2017]. Inferences as to the source of El Dorado sediments were based on geochemical trends from APXS analyses of the disturbed El Dorado sediment. Data showed enrichments in Mg, K, and Ni and depletions in Fe, Mn, Ca, Cr, and Zn compared to the primitive, olivine-bearing Adirondack class basalts nearby in Gusev crater [*Arvidson et al.*, 2006; *Ming et al.*, 2008]. These differences suggest at least three sources for the El Dorado ripple field: (1) local Algonquin Class materials (mafic to ultramafic rocks rich in olivine), (2) Adirondack olivine-rich basalts from the Gusev plains, and (3) additional materials, such as air fall dust, from unidentified locations [*Ming et al.*, 2008]. The Gobabeb mineralogy also points multiple sediment sources due to disequilibrium among olivine, augite, and pigeonite compositions. Mössbauer analyses of the undisturbed El Dorado soil show an Fe_{ol} to Fe_{pyx} ratio of ~1.5, higher than average Gusev low-dust soils (~1.1), but significantly lower than Gobabeb (~2.4). The ratios likely reflect the increased olivine abundance observed at the Gobabeb site and may change in areas where pyroxene is more abundant.

Overall, analyses of Gale soils reveal similar crystalline phase abundances for the Rocknest and Gobabeb sediments in addition to nearly identical major mineral chemistries, excluding plagioclase. These eolian samples, along with the ancient Stimson and MER eolian deposits, reveal similar compositions among sediments widely distributed in space and time.

5. Conclusions

Gobabeb is dominated by basaltic minerals (~58 wt %) and X-ray amorphous phases (~42 wt %). Plagioclase (~37 wt %), olivine (~26 wt %), and two Ca-Mg-Fe pyroxenes (~33 wt % total) account for most of the mass of the crystalline component. Minor phases include magnetite, quartz, hematite, and anhydrite. Cell vibration experiments show that the major phases (i.e., olivine, pyroxene, and plagioclase) are also the largest in grain size. The smallest grains are hematite and anhydrite. The calculated composition of the X-ray amorphous component suggests that several phases comprise the amorphous material. Dominated by SiO_2 (~50 wt %), FeO_T (~20 wt %), Al_2O_3 (~8 wt %), and SO_3 (~7 wt %), proposed phases include maskelynite, amorphous silica, nanophase iron oxides, and sulfates. Basaltic soils in Gale, Meridiani, and Gusev have similar chemical compositions, and modeled mineralogies at the MER sites show similar phase abundances. CheMin's mineralogical analysis of the Gobabeb data set provides an opportunity to ground-truth orbital observations. The predicted mineralogy of the Bagnold Dune Field based on VNIR and MIR orbital spectral measurements shows high fidelity to in situ CheMin mineralogical analyses. This unique ground truth comparison can be used to validate and improve upon spectral models of crystalline phases, and the calculated amorphous composition can provide information about amorphous materials which may be ambiguous or poorly constrained in orbital measurements.

Acknowledgments
This research was supported by the NASA Mars Science Laboratory Mission (grant NNX11AP82A) and by NASA Headquarters under the NASA Earth and Space Science Fellowship Program (grant NNX16AL41H). We would like to acknowledge the support of JPL engineering and the Mars Science Laboratory operations team. All data used in this manuscript are available at the NASA Planetary Data System Geosciences Node. Any opinions, findings, or recommendations expressed herein are those of the authors and do not necessarily reflect the views of the National Aeronautics and Space Administration.

References

Agee, C. B., N. Muttik, K. Zeigler, F. M. McCubbin, P. Rochette, and J. Gattacceca (2014), Discovery of a new Martian meteorite type: Augite basalt-Northwest Africa 8159, Abstract 2036.

Anderson, R. B., and J. F. Bell (2010), Geologic mapping and characterization of Gale Crater and implications for its potential as a Mars Science Laboratory landing site, *Mars*, *5*, 76–128.

Anderson, R. C., et al. (2012), Collecting samples in Gale Crater, Mars: An overview of the Mars Science Laboratory sample acquisition, sample processing and handling system, *Space Sci. Rev.*, *170*(1–4), 5775, doi:10.1007/s11214-012-9898-9.

Arvidson, R. E., et al. (2006), Overview of the Spirit Mars Exploration Rover Mission to Gusev Crater: Landing site to Backstay Rock in the Columbia Hills, *J. Geophys. Res.*, *111*, E02S01, doi:10.1029/2005JE002499.

Banham, S. G., S. Gupta, D. M. Rubin, J. A. Watkins, D. Y. Sumner, J. P. Grotzinger, K. W. Lewis, K. S. Edgett, L. A. Edgar, and K. M. Stack (2016), Reconstruction of an ancient eolian dune field at Gale Crater, Mars: Sedimentary analysis of the Stimson Formation, *LPSC XLVII*, Abstract 2346.

Bish, D., et al. (2013), X-ray diffraction results from Mars Science Laboratory: Mineralogy of Rocknest at Gale Crater, *Science*, *341*(6153), 1238932, doi:10.1126/science.1238932.

Blake, D., et al. (2012), Characterization and calibration of the CheMin mineralogical instrument on Mars Science Laboratory, *Space Sci. Rev.*, doi:10.1007/s11214-012-9905-1.

Blake, D., et al. (2013), Curiosity at Gale Crater, Mars: Characterization and analysis of the Rocknest sand shadow, *Science*, *341*(6153), 1239505, doi:10.1126/science.1239505.

Boynton, W., et al. (2009), Evidence for calcium carbonate at the Mars Phoenix landing site, *Science*, *325*(5936), 61–64, doi:10.1126/science.1172768.

Bridges, J. C., and P. H. Warren (2006), The SNC meteorites: Basaltic igneous processes on Mars, *J. Geol. Soc.*, *163*, 229–251.

Bridges, N. T., and B. L. Ehlmann (2017), The Mars Science Laboratory (MSL) Bagnold Dunes campaign, Phase I: Overview and introduction to the special issue, *J. Geophys. Res. Planets*, *122*, doi:10.1002/2017JE005401.

Cannon, K., B. Sutter, D. Ming, W. Boynton, and R. Quinn (2012), Perchlorate induced low temperature carbonate decomposition in the Mars Phoenix Thermal and Evolved Gas Analyzer (TEGA), *Geophys. Res. Lett.*, *39*, L13203, doi:10.1029/2012GL051952.

Chipera, S., and D. Bish (2013), Fitting full X-ray diffraction patterns for quantitative analysis: A method for readily quantifying crystalline and disordered phases, *Adv. Mater. Phys. Chem.*, *03*(01), 47, doi:10.4236/ampc.2013.31A007.

Clark, B., A. Baird, R. Weldon, D. Tsusaki, L. Schnabel, and M. Candelaria (1982), Chemical composition of Martian fines, *J. Geophys. Res.*, *87*, 10,059–10,067, doi:10.1029/JB087iB12p10059.

Cousin, A., et al. (2017), Geochemistry of the Bagnold dune field as observed by ChemCam and comparison with other aeolian deposits at Gale crater, *J. Geophys. Res. Planets*, *122*, doi:10.1002/2017JE005261.

Day, M., and G. Kocurek (2016), Observations of an aeolian landscape: From surface to orbit in Gale Crater, *Icarus*, *280*, 37–71.

Dera, P., K. Zhuravlev, V. Prakapenka, M. Rivers, G. Finkelstein, O. Grubor-Urosevic, O. Tschauner, S. Clark, and R. Downs (2013), High pressure single-crystal micro X-ray diffraction analysis with GSE_ADA/RSV software, *High Pressure Res.*, *33*(3), 466–484, doi:10.1080/08957959.2013.806504.

Downs, R. T., and MSL Science Team (2015), Determining mineralogy on Mars with the CheMin X-ray diffractometer, *Elements*, *11*(1), 45–50, doi:10.2113/gselements.11.1.45.

Ehlmann, B., and J. Buz (2015), Mineralogy and fluvial history of the watersheds of Gale, Knobel, and Sharp craters: A regional context for the Mars Science Laboratory Curiosity's exploration, *Geophys. Res. Lett.*, *42*, 264–273, doi:10.1002/2014GL062553.

Ehlmann, B. L., et al. (2017), Chemistry, mineralogy, and grain properties at Namib and High Dunes, Bagnold Dune Field, Gale crater, Mars: A synthesis of Curiosity rover observations, *J. Geophys. Res. Planets*, *122*, doi:10.1002/2017JE005267.

Gellert, R., B. Clark, and M. S. L. Team (2015), In situ compositional measurements of rocks and soils with the Alpha Particle X-ray Spectrometer on NASA's Mars rovers, *Elements*, *11*(1), 39–44, doi:10.2113/gselements.11.1.39.

Glotch, T. D., and J. L. Bandfield (2006), Determination and interpretation of surface and atmospheric Miniature Thermal Emission Spectrometer spectral end-members at the Meridiani Planum landing site, *J. Geophys. Res.*, *111*, E12S06, doi:10.1029/2005JE002671.

Greeley, R., and J. D. Iversen (1985), *Wind as a Geological Process*, 333 pp., Cambridge Univ. Press, New York.

Grotzinger, J. P., et al. (2015), Deposition, exhumation, and paleoclimate of an ancient lake deposit, Gale Crater, Mars, *Science*, *350*(6257), doi:10.1126/science.aac7575.

Hecht, M. H., et al. (2009), Detection of perchlorate and the soluble chemistry of Martian soil at the Phoenix lander site, *Science*, *325*(5936), 64–67, doi:10.1126/science.1172466.

Hobbs, S., D. Paull, and M. Bourke (2010), Aeolian processes and dune morphology in Gale Crater, *Icarus*, *210*(1), 102–115, doi:10.1016/j.icarus.2010.06.006.

Johnson, J. R., et al. (2017), Visible/near-infrared spectral diversity from in situ observations of the Bagnold dune field sands in Gale Crater, Mars, *J. Geophys. Res. Planets*, *122*, doi:10.1002/2016JE005187.

Lafuente, B., R. T. Downs, H. Yang, and N. Stone (2015), The power of databases: The RRUFF project, pp. 1–30, De Gruyter.

Lane, M., and P. Christensen (2013), Determining olivine composition of basaltic dunes in Gale Crater, Mars, from orbit: Awaiting ground truth from Curiosity, *Geophys. Res. Lett.*, *40*, 3517–3521, doi:10.1002/grl.50621.

Lapotre, M., et al. (2016), Large wind ripples on Mars: A record of atmospheric evolution, *Science*, *353*(6294), 55–58, doi:10.1126/science.aaf3206.

Lapotre, M. G. A., B. L. Ehlmann, S. E. Minson, R. E. Arvidson, F. Ayoub, A. A. Fraeman, R. C. Ewing, and N. T. Bridges (2017), Compositional variations in sands of the Bagnold Dunes, Gale Crater, Mars, from visible-shortwave infrared spectroscopy and comparison with ground truth from the Curiosity rover, *J. Geophys. Res. Planets*, *122*, doi:10.1002/2016JE005133.

Lindsley, D. H. (1983), Pyroxene thermometry, *Am. Mineral.*, *68*(5–6), 477–493.

Mahaffy, P., C. Webster, M. Cabane, and P. Conrad (2012), The sample analysis at Mars investigation and instrument suite, *Space Sci. Rev.*, *170*(1–4), 401–478, doi:10.1007/s11214-012-9879-z.

Maurice, S., R. Wiens, and M. Saccoccio (2012), The ChemCam instrument suite on the Mars Science Laboratory (MSL) rover: Science objectives and mast unit description, *Space Sci. Rev.*, *170*(1–4), 96–166, doi:10.1007/s11214-012-9912-2.

McSween, H., I. McGlynn, and D. Rogers (2010), Determining the modal mineralogy of Martian soils, *J. Geophys. Res.*, *115*, E00F12, doi:10.1029/2010JE003582.

McSween, H. Y., and A. H. Treiman (1998), Martian meteorites, *Rev. Mineral. Geochem.*, *36*(1), 6–1–6–54.

Milliken, R., J. Grotzinger, and B. Thomson (2010), Paleoclimate of Mars as captured by the stratigraphic record in Gale Crater, *Geophys. Res. Lett.*, *37*, L04201, doi:10.1029/2009GL041870.

Ming, D. W., et al. (2006), Geochemical and mineralogical indicators for aqueous processes in the Columbia Hills of Gusev crater, Mars, *J. Geophys. Res.*, *111*, E02S12, doi:10.1029/2005JE002560.

Ming, D. W., et al. (2008), Geochemical properties of rocks and soils in Gusev Crater, Mars: Results of the Alpha Particle X-ray Spectrometer from Cumberland Ridge to Home Plate, *J. Geophys. Res.*, *113*, E12S39, doi:10.1029/2008JE003195.

Morris, R. V., et al. (2004), Mineralogy at Gusev Crater from the Mossbauer spectrometer on the Spirit rover, *Science*, *305*(5685), 833–836, doi:10.1126/science.1100020.

Morris, R. V., et al. (2006a), Mössbauer mineralogy of rock, soil, and dust at Gusev crater, Mars: Spirit's journey through weakly altered olivine basalt on the plains and pervasively altered olivine basalt on the plains and pervasively altered basalt in the Columbia Hills, *J. Geophys. Res.*, *111*, E02S13, doi:10.1029/2005JE002584.

Morris, R. V., et al. (2006b), Mössbauer mineralogy of rock, soil, and dust at Meridiani Planum, Mars: Opportunity's journey across sulfate-rich outcrop, basaltic sand and dust, and hematite lag deposits, *J. Geophys. Res.*, *111*, E12S15, doi:10.1029/2005JE002584.

Morris, R. V., et al. (2008), Iron mineralogy and aqueous alteration from Husband Hill through Home Plate at Gusev Crater, Mars: Results from the Mössbauer instrument on the Spirit Mars Exploration Rover, *J. Geophys. Res.*, *113*, E12S42, doi:10.1029/2008JE003201.

Morris, R. V., E. B. Rampe, T. G. Graff, P. D. Archer Jr., L. Le, D. W. Ming, and B. Sutter (2015), Transmission X-ray diffraction (XRD) patterns relevant to the MSL CheMin Amorphous component: Sulfates and silicates, *LPSC XLVI* Abstract 2434.

Morris, R. V., et al. (2016), Silicic volcanism on Mars evidenced by tridymite in high-SiO2 sedimentary rock at Gale Crater, *Proc. Natl. Acad. Sci.*, *113*(26), 7071–7076, doi:10.1073/pnas.1607098113.

Morrison, S. M., et al. (2017), Crystal chemistry of Martian minerals from Bradbury landing through Naukluft Plateau, Gale Crater, Mars, *Am. Min.*, doi:10.2138/am-2018-6124.

O'Connell-Cooper, C. D., J. G. Spray, L. M. Thompson, R. Gellert, J. A. Berger, N. I. Boyd, E. D. Desouza, G. M. Perrett, M. Schmidt, and S. J. VanBommel (2017), APXS-derived chemistry of the Bagnold dune sands: Comparisons with Gale crater soils and the global martian average, *J. Geophys. Res. Planets*, *122*, doi:10.1002/2017JE005268.

Rampe, E. B., et al. (2017), Mineralogy of an ancient lacustrine mudstone succession from the Murray formation, Gale Crater, Mars, Earth Planet. *Sci. Lett.*, *471*, 172–185, doi:10.1016/j.epsl.2017.04.021.

Rieder, R., T. Economou, H. Wänke, A. Turkevich, J. Crisp, J. Brückner, G. Dreibus, and H. McSween (1997), The chemical Composition of Martian soil and rocks returned by the mobile Alpha Proton X-ray Spectrometer: Preliminary results from the X-ray mode, *Science*, *278*(5344), 1771–1774, doi:10.1126/science.278.5344.1771.

Rogers, A., and O. Aharonson (2008), Mineralogical composition of sands in Meridiani Planum determined from Mars Exploration Rover data and comparison to orbital measurements, *J. Geophys. Res.*, *113*, E06S14, doi:10.1029/2007JE002995.

Rogers, A., and J. Bandfield (2009), Mineralogical characterization of Mars Science Laboratory candidate landing sites from THEMIS and TES data, *Icarus*, *203*(2), 437–453, doi:10.1016/j.icarus.2009.04.020.

Santos, A., C. Agee, F. McCubbin, C. Shearer, P. Burger, R. Tartèse, and M. Anand (2015), Petrology of igneous clasts in Northwest Africa 7034: Implications for the petrologic diversity of the Martian crust, *Geochim. Cosmochim. Acta*, *157*, 56–85, doi:10.1016/j.gca.2015.02.023.

Sautter, V., et al. (2015), In situ evidence for continental crust on early Mars, *Nat. Geosci.*, *8*, 605–609, doi:10.1038/NGEO2474.

Seelos, K., F. Seelos, C. Viviano-Beck, S. Murchie, R. Arvidson, B. Ehlmann, and A. Fraeman (2014), Mineralogy of the MSL Curiosity landing site in Gale Crater as observed by MRO/CRISM, *Geophys. Res. Lett.*, *41*, 4880–4887, doi:10.1002/2014GL060310.

Silvestro, S., D. A. Vaz, R. C. Ewing, A. P. Rossi, L. K. Fenton, T. I. Michaels, J. Flahaut, and P. E. Geissler (2013), Pervasive aeolian activity along rover Curiosity's traverse in Gale Crater, Mars, *Geology*, *41*(4), 483–486, doi:10.1130/G34162.1.

Silvestro, S., D. A. Vaz, H. Yizhaq, and F. Esposito (2016), Dune-like dynamic of Martian Aeolian large ripples, *Geophys. Res. Lett.*, *43*, 8384–8389, doi:10.1002/2016GL070014.

Sullivan, R., et al. (2008), Wind-driven particle mobility on Mars: Insights from Mars Exploration Rover observations at "'El Dorado'" and surroundings at Gusev crater, *J. Geophys. Res.*, *113*, E06S07, doi:10.1029/2008JE003101.

Sutter, B., W. V. Boynton, D. W. Ming, P. B. Niles, R. V. Morris, D. C. Golden, H. V. Lauer, C. Fellows, D. K. Hamara, and S. A. Mertzman (2012), The detection of carbonate in the Martian soil at the Phoenix Landing site: A laboratory investigation and comparison with the Thermal and Evolved Gas Analyzer (TEGA) data, *Icarus*, *218*(1), 290–296, doi:10.1016/j.icarus.2011.12.002.

Sutter, B., et al. (2017), Evolved gas analyses of sedimentary rocks and eolian sediment in Gale Crater, Mars: Results of the Curiosity Rover's Sample Analysis at Mars (SAM) instrument from Yellowknife Bay to the Namib dune, *J. Geophys. Res. Planets*, *122*, doi:10.1002/2016JE005225.

Thompson, L. M., et al. (2016), Potassium-rich sandstones within the Gale impact crater, Mars: The APXS perspective, *J. Geophys. Res. Planets*, *121*, 1981–2003, doi:10.1002/2016JE005055.

Treiman, A. H. (2005), The nakhlite meteorites: Augite-rich igneous rocks from Mars, *Chem. Erde-Geochem.*, *65*(3), 203–270.

Udry, A., N. Lunning, H. McSween, and R. Bodnar (2014), Petrogenesis of a vitrophyre in the Martian meteorite breccia NWA 7034, *Geochim. Cosmochim. Acta*, *141*, 281–293, doi:10.1016/j.gca.2014.06.026.

Yen, A., et al. (2005), An integrated view of the chemistry and mineralogy of Martian soils, *Nature*, *436*(7047), 49–54, doi:10.1038/nature03637.

Yen, A. S., et al. (2006), Nickel on Mars: Constraints on meteoritic material at the surface, *J. Geophys. Res.*, *111*, E12S11, doi:10.1029/2006JE002797.

Yen, A. S., et al. (2017), Multiple stages of aqueous alteration along fractures in mudstone and sandstone strata in Gale Crater, Mars, *Earth Planet. Sci. Lett.*, *471*, 186–198, doi:10.1016/j.epsl.2017.04.033.